RSC Advances

PAPER

View Article Online
View Journal | View Issue

Cite this: *RSC Adv.*, 2019, **9**, 13348

Si, Sr, Ag co-doped hydroxyapatite/TiO_2 coating: enhancement of its antibacterial activity and osteoinductivity

Haixia Qiao,[a] Guiqin Song,[a] Yong Huang, *[a] Hao Yang, [c] Shuguang Han,[b] Xuejiao Zhang,[a] Zhenhui Wang,[e] Jing Ma,[e] Xiaopei Bu[e] and Li Fu[d]

A multifaceted coating with favourable cytocompatibility, osteogenic activity and antibacterial properties would be of great significance and value due to its capability for improving osseointegration and alleviating prosthesis loosening. This study marks the first report on the coating of TiO_2 nanotubular (TNT) arrays with Sr-and-Si-substituted hydroxyapatite (SSHA) endowed with antibacterial characteristics using silver ions. This TNT layer coated with Ag-substituted SSHA (SSAgHA) formed a composite coating with an interconnected microporous structure and a homogeneous distribution of Sr, Si and Ag; such a coating promoted cell adhesion and osteogenic potential. The anchoring effect of the TNT layer improved the adhesion strength of the SSAgHA/TNT coating to 16.9 ± 3.1 MPa, which was higher than the 15 MPa set in the ISO standard 13 779-4:2002. Moreover, the bio-corrosion resistance of the underlying Ti substrate was greatly enhanced by the composite coating. Hydroxyapatite (HA) and SSAgHA coatings provided a suitable environment for the adhesion, spreading and proliferation of mouse osteoblasts. The SSAgHA coating excellently inhibited bacterial activity and enhanced osteoinductivity with higher osteogenic differentiation compared with the HA coating. Sr and Si dopants increased the expression levels of the genes related to osteogenesis and successfully offset the potential cytotoxicity of Ag ions. Super-osteoinductivity was attributed to the rough and superhydrophilic surface of the composite coating. Therefore, the present study demonstrated the potential of the electrodeposited SSAgHA/TNT composite coating as a promising metallic implant with great intrinsic antibacterial activity and osteointegration ability.

Received 15th February 2019
Accepted 15th April 2019

DOI: 10.1039/c9ra01168d

rsc.li/rsc-advances

1. Introduction

In view of the rapid development of orthomorphia, frequently occurring fracture and joint degeneration and age-related bone defects, artificial orthopaedic implants are increasingly in demand.[1] High mechanical strength, low elasticity and reasonable biocompatibility have made metallic biomaterials clinically useful in fixing bone fractures and implanting joint prostheses.[2] For example, titanium (Ti) and its alloys have been extensively considered for orthopaedic applications.[3] However, the bio-inertness of many biometals impedes the progress of the healing process, and their inherent lack of antibacterial characteristics increases the chance of bacterial infection, which can lead to implant failure.[4,5]

The abuse of antibiotics during common clinical treatment of implant-related bacterial infections may lead to bacterial resistance.[6] Moreover, antibiotics can function poorly therapeutically against a bacterial biofilm that has already formed on the surface of an implant. Therefore, viable approaches to bacterial infections are the design of anti-adhesive surfaces, the release of antimicrobial agents, the use of antibacterial coatings and the application of nanostructured materials and molecules, which contain antibiotics that can interfere with bacterial biofilms.[7–10] The incorporation of inorganic antimicrobial agents into coatings leads to bacterial death, which avoids the development of drug resistance.[11,12] A well-known example of antimicrobial agents is Ag, which acts against bacteria by being released as ions.[13,14] However, these methods suffer from some drawbacks; for example, released inorganic nanoparticles can cause toxicity,[11] and Ag ions in large concentrations can induce cytotoxicity.[15] Furthermore, most antibacterial methods cannot improve the osteogenetic ability of bioinert implants. Implant loosening and failure can also occur because of a weak bond between implants and new bone tissues;[12,16] therefore, the development of new coatings that

[a]College of Lab Medicine, Hebei North University, Zhangjiakou 075000, China. E-mail: xfpang@aliyun.com; Tel: +86 313 4029270
[b]School of Life Science and Technology, University of Electronic Science and Technology of China, Chengdu 610054, China
[c]Key Laboratory for Green Chemical Process of Ministry of Education, School of Environmental Ecology and Biological Engineering, Wuhan Institute of Technology, Wuhan, 430205, China
[d]College of Materials and Environmental Engineering, Hangzhou Dianzi University, Hangzhou 310018, China
[e]No. 81st Group Military Hospital of PLA Army, Zhangjiakou 075000, China

simultaneously have good osteoinductivity and antimicrobial abilities is in demand.[12]

Having a chemical composition almost similar to natural bone and tooth, hydroxyapatite (HA) has great biocompatibility and osteoinductivity.[17] Different trace elements (Sr, Si, Mn, Mg, CO_3^{2-}, F and Zn) with specific biological properties are usually found in biological apatites, which form in biological conditions.[18] The bioactivity of an implant—its antibacterial, anti-inflammatory, anti-osteoporotic and angiogenic properties—can be tuned through selected doping.[9] Several biologically active ions, such as Si and Sr, have been regarded as dopants because of their natural presence in native bone tissues and can beneficially influence the biological response of osteoblasts.[17,19,20] These trace elements physiologically function as enzymatic co-factors and signalling molecules;[19,20] being essential for early embryonic bone formation, Si is not present in mature bone tissues[21] that are directly affected by Sr, another trace element that is linked to osteoclast and osteoblast differentiation.[17] Therefore, Si and Sr co-substitution of HA may enhance osteoblast proliferation and differentiation more than what a single Si or Sr substitution of HA can achieve; this hypothesis still demands a good deal of research. Published information about the simultaneous effects of Sr, Si and Ag on surface features, antibacterial activity and biological performance of HA-based coatings is lacking. To test the aforementioned hypothesis further, we co-doped HA with Sr, Si and Ag to make a coating that benefits from the combined capabilities of Sr and Si for the promotion of osteogenesis and of Ag for the inhibition of bacterial growth. To the best of our knowledge, research on single-ion doping and co-doping of two or three ions has rarely been reported.

Several deposition methods have already been investigated to produce co-substituted Ca–P coatings,[16] including plasma spraying,[24] sol–gel technique,[25] pulsed laser deposition,[26] magnetron sputtering[27] and electrophoretic deposition.[28] Herein, we report for the first time the fabrication of a composite coating of a layer of TiO_2 nanotube (TNT) arrays coated with the Si–Sr–Ag-substituted HA (SSAgHA). The TNT layer enhances the electrochemical resistance of the coating to minimise wear-induced leaching.[16] The electrochemical deposition (ED) technique was employed to synthesise the SSAgHA coating. To change the adhesion and differentiation of osteoblasts, the specific surface area, surface roughness and wettability of implants were tuned using ED; therefore, ED is particularly useful for the deposition of HA coatings.[29,30] The collective effects of co-dopants (Sr^{2+}, Ag^{+} and Si^{4+}) on the wettability, corrosion resistance, crystalline phase, antimicrobial activity and biocompatibility of the coatings were also studied.

2. Materials and methods

2.1 Preparation of TiO_2 nanotubes on Ti substrate

Samples with a size of $10 \times 10 \times 1.1$ mm^3 were cut from pure Ti sheet (99.9%, ASTM F67 Grade 1). Different grades of silicon carbide papers (240-2000 grit) were used to abrade the samples mechanically. The samples were chemically polished for 30 s in a 3 : 1 solution of HNO_3 and HF. Thereafter, ultrasonic cleaning was performed in acetone, ethanol and deionised water. Before being coated, the samples were anodised at a constant voltage of 20 V and 25 °C for 60 min in an ethylene-glycol-based electrolyte containing 0.5 wt% NH_4F. Finally, the anodised samples were annealed at 550 °C for 1 h to crystallise the amorphous TiO_2 into the rutile phase.

2.2 Synthesis of SSAgHA/TNT coatings

After the substrates were prepared for coating, SSAgHA/TNT coatings were electrodeposited according to our previous report;[31] the samples were used as the cathode, and the anode was made out of Pt. Analytical grade $Ca(NO_3)_2$, $NH_4H_2PO_4$, $AgNO_3$ and $Sr(NO_3)_2$ were used as the sources of Ca^{2+}, PO_4^{3-}, Ag^{+} and Sr^{2+}, respectively. The above electrolyte was supplemented with 1 wt% nano-SiO_2 (15 ± 5 nm) solution, and the pH of the solution was set to 4.2. The molar ratio of Ag to the sum of Ca + Ag and the molar ratio of Ag to Ca + Ag were both 0.1. The distance between the cathode and anode was fixed at 1.5 cm. Deposition was performed with an electrochemical workstation (CHI 660E, China) operating at 0.9 mA cm^{-2} and 65 °C for 0.5 h. After being removed from the electrolyte, the coated samples were dried at 65 °C for 2 h. Finally, they were annealed at 450 °C for 2 h.

2.3 Characterisation of SSAgHA/TNT coatings

The surface morphologies of the coated samples were investigated by scanning electron microscopy (SEM; JEOL JSM-7500F, Tokyo, Japan) with energy-dispersive spectrometry (EDS). The crystalline phases of the samples were examined *via* X-ray diffraction (XRD) (Rigaku D/Max-2500/PC, Tokyo, Japan) using Cu Kα radiation ($l = 1.541874$ Å) with scanning from 5° to 80° with a rate of 0.06° s^{-1}. Functional groups were analysed *via* Fourier transform infrared (FTIR) spectrometry (Nicolet iS5, USA) within the range of 4000–500 cm^{-1} at a resolution of 4 cm^{-1}. The chemical states were determined by X-ray photoelectron spectroscopy (XPS; Thermo ESCALAB 250XI) with Al Kα radiation (1486.6 eV). The surface roughness of the samples was measured with an atomic force microscope (AFM, Bruker, Dimension Icon, USA). A universal testing machine (AG-10TA, Shimadzu) (ASTMF1044-05) was used to measure the adhesion strength of the SSAgHA/TNT coating.[16] A contact angle instrument (Easy Drop Instrument, DSA 100, Kruess, Germany) with deionised water as medium was used to measure the contact angles.[31]

2.4 Ion release measurements

The concentrations of the released Ca, Ag, Si and Sr ions were measured by inductively coupled plasma mass spectrometry (ICP-MS; 7700, Agilent Technologies Inc., USA). To this end, the SSAgHA-coated Ti samples were incubated at 37 °C for 14 days in 10 mL of PBS (Gibco, USA) at pH 7.4; the buffer was periodically renewed every 24 h.[32] The ion contents of each collected buffer were measured *via* ICP-MS, and the cumulative concentrations of released Ca, Ag, Si and Sr ions at each time interval were calculated.

2.5 Electrochemical corrosion resistance analysis

The impedance and polarisation data were obtained from the bare and coated substrates using the electrochemical workstation (VertexOne, Netherlands). The standard three-electrode system had the sample as its working electrode, the standard calomel electrode as its reference and a platinum rode as its counter electrode. The open-circuit potential (E_{OCP}) was established by immersing the Cp-Ti, HA, AgHA and SSAgHA samples in an electrolyte of Kukubo's simulated body fluid (SBF) at 37 °C. Electrochemical impedance spectroscopy (EIS) was performed in the high-to-low frequency region, and the resultant data were expressed as Nyquist plots. Potentiodynamic polarisation measurements were conducted within the range of E_{OCP} ±0.25 V, and the obtained data were expressed as Tafel plots, which helped determine the corrosion current (i_{corr}) and corrosion potential (E_{corr}).

2.6 Antibacterial activity

2.6.1 Inhibition zone analysis. Quantity and quality assessments of the antibacterial properties of the SSAgHA-coated Ti samples were performed on Gram-positive *Staphylococcus aureus* (ATCC 25923). The qualitative assessment, inhibition zone measurement, was based on the disk diffusion method.[31] Nutrient agar plates were inoculated with 1 mL of a bacterial suspension that contained about 10^7 colony-forming units (CFUs) of bacteria per millilitre. Disks of HA, Ag-doped HA (AgHA), Sr–Ag-doped HA (SrAgHA) and SSAgHA were incubated at 37 °C for 36 h. The inhibition zone around each sample was photographed.

2.6.2 Spread plate. Bacteria were cultured in Luria–Bertani (LB) culture medium. LB broth and LB agar plates were sterilised by autoclaving at 121 °C for 15 min. For the sake of averaging, three samples were tested in each group. The samples were placed on a 24-well plate, and 400 μL of the *S. aureus* suspension (1×10^7 CFU mL^{-1}) that was diluted in sterile PBS broth was incubated in a biological safety cabinet at 37 °C for 12 h. A 100-fold dilution of sterile PBS was used to dilute the *S. aureus* suspension in each hole. Subsequently, 20 μL of the diluted *S. aureus* suspension from each hole was spread on LB agar plates and incubated in the oven at 37 °C for 24 and 36 h. Antibacterial activity was calculated as $R = (B - A)/B \times 100\%$,[23] where R is the antibacterial rate, and A and B are the mean numbers of viable bacteria (CFU) on the Ag-doped HA and pure HA samples, respectively.

2.7 Osteoblast culture and evaluation

We used mouse calvarial cell line MC3T3-E1 (West China School of Medicine). The culture medium of the cells on a dish was an atmosphere of 5% CO_2 at 37 °C in an incubator and contained α-MEM (HyClone) supplemented with 1% penicillin–streptomycin (HyClone) and 10% foetal bovine serum (FBS). Sterilised PBS and trypsin/ethylenediaminetetraacetic acid (EDTA, Sigma) were used to remove dead cells. For later use, the culture was diluted to a density of 1×10^5 cells per mL.

In this study, 3×10^4 cells per well was the density of the osteoblasts in the 24-well culture plates. The number of adherent cells (after 1 and 2 h of culture) and cell proliferation rates (after 1, 4 and 7 days of culture) were assessed by using the Alamar Blue assay as instructed by the manufacturer. After 1 day of culture, the samples with attached osteoblast cells were rinsed twice in PBS. The samples were fixed in 2.5% glutaraldehyde in PBS at room temperature and air-dried after dehydration in a graded ethanol series. After being sputter-coated with gold, they were examined *via* field emission scanning electron microscopy (FE-SEM).

The distribution and attachment behaviour of the cells on the samples were further visualised through fluorescence microscopy (model SMZ745/745T; Nikon Corporation, Tokyo, Japan). Cell live/dead staining determined the viable and non-viable MC3T3-E1 cells after 3 days.[33] The samples were rinsed in PBS, and the supernatant was replaced with 1 mL of the PBS solution that contained 2 μL (1 mg mL^{-1}) of calcein AM and 2 μL (1 mg mL^{-1}) of propidium iodide (Sigma-Aldrich). To visualise the cytoskeleton (actin fibres) and nuclei, the cells were washed with PBS twice and then fixed with 3.6% formaldehyde (Sigma-Aldrich) for 30 min at room temperature. After 30 min of staining in 50 μL (6.6 μg mL^{-1}) of phalloidin (Phalloidin Alexa Fluor® 488 Phalloidin, Thermo Fisher Scientific), they were rinsed in PBS twice. Final staining was performed in 50 μL (2.5 μg mL^{-1}) of DAPI (Sigma-Aldrich).

2.8 Quantitative reverse-transcription polymerase chain reaction

Osteogenic differentiation was assessed. The expression levels of the genes that were implicated in bone matrix synthesis were measured *via* quantitative reverse-transcription polymerase chain reaction (qRT-PCR). The 14 day-cultured osteoblasts that had been seeded at a density of 3×10^4 cells per well were harvested by TRIzol (Invitrogen, Milan, Italy). An RNeasy Micro Kit was used to extract and clean total mRNA. After the on-column DNase digestion step, the residual genomic DNA was removed with an RNase-Free DNase Set (Qiagen). RNA was quantified on a Qubit quantitation platform (Invitrogen, Cergy Pontoise, France). RNA quality was evaluated with 1% agarose gel electrophoresis and optical density measurements. Thereafter, reverse transcription was performed using a high-capacity reverse transcription kit (Applied Biosystems) for real-time PCR experiments. The cDNA and frozen RNA extracts were stored at −20 °C and −80 °C, respectively. The specificity and efficiency of the primers were tested for the amplification of alkaline phosphatase (ALP), type I collagen (Col-I), osteocalcin (OCN), osteopontin (OPN), bone morphogenetic protein-2 (BMP-2) and runt-related transcription factor 2 (RUNX2) (Table 1). Glyceraldehyde-3-phosphate dehydrogenase (GAPDH) was the internal control (IC). The relative expression level of each mRNA was calculated using the $2^{-\Delta\Delta C_t}$ method.

2.9 Statistical analysis

According to Kruskal–Wallis one-way ANOVA test, the results of at least three experiments were calculated as the mean ± standard deviation.

Table 1 Primers used in real-time PCR

	Sequences	
Target gene	Forward primer (5′ → 3′)	Reverse primer (5′ → 3′)
ALP	TACACGGACACTGAGATGCGCT	TCGTGCATTATCTGATAGGTGA
BMP-2	GCTAAACTTGACGACGCTCGT	CTGCTCGGTTCCCGTTA
Col-I	CTAAAGAATGACTACAGCTA	TCCACCCCTAGTGCGTTGCT
OCN	CTGTTTAGGGTGTGTGTCGC	TAGCGAGGCAACGAGATCAA
OPN	TCTGGAGAGGAGTGAAGCTC	AGGGAAGCGTCAATCTTAAG
RUNX2	CTGTCCCTCCCTCACCCCGT	GACGCCTGCTGTCTTCTGTAG
GAPDH (IC)	CCTCCAGGAACTCTCCTCAG	GTATGAGAGCGCAGCCAACGG

3. Results and discussion

3.1 Characterisation of TNT

Fig. 1 shows the schematic of Si–Sr–Ag co-doped HA/TiO_2 coatings with antibacterial activity and cytocompatibility fabricated by electrochemical deposition combined with anodization. Antibacterial activity and *in vitro* cell viability studies showed that the biological properties of the SSAgHA/TNT-coated Ti were appropriate for orthopaedic applications.

Fig. 2a and b display the top and cross-sectional FESEM views of the TNT that formed on the surface of the Ti substrate. The homogenously porous structure of the TNT layer on the Ti substrate favoured the infiltration of the SSAgHA crystals. XRD tests were used to examine the purity and crystalline structure. The phase compositions of the anodised samples were reported in our previous publications;[31,34] all the reflections reproduced the standard patterns, including JCPDS#005-0682 for the Ti substrate and #021-1276 for rutile (Fig. 2c). The vibrational mode of Ti–O bending formed the band at 810 cm^{-1} in the FT-IR spectra of the anodised Ti surface (Fig. 2d).[35] When balanced, the three processes of oxide growth, field-assisted dissolution and chemical dissolution of the oxide layer in the presence of fluoride ions lead to the formation of titanium nanotubes during the anodization of the Ti substrate.[36] The introduction of an intermediate layer of nanotubular arrays of TiO_2 before the application of the CaP-based coatings can favourably enhance adhesive strength between the coating and Ti substrate.[29,36,37]

3.2 Characterisation of as-deposited SSAgHA/TNT coatings

Fig. 3a shows the XRD data of the HA-, AgHA- and SSAgHA-coated samples. The patterns agreed with that of the HA phase (JCPDS no. 09-0432) with a pronounced 002 preferred orientation. The high crystallinity of the samples was evident from the sharpness of the diffraction peaks. The diffraction pattern of the SSAgHA-coated sample included the peaks attributed to the pre-treated Ti (rutile and Ti) and peaks related to the HA phase. These results suggested that the trace Ag, Si and Sr dopants did not make any new phase within HA. Interestingly, the incorporation of SiO_4^{4-}, Ag^+ and Sr^{2+} ions into the HA lattice did not result in any lattice distortion, impediment to crystal growth or decline in crystallinity.

Fig. 3b presents the FTIR spectra of the coatings in the range of 500–4000 cm^{-1}. The peaks at 962 and 1000–1200 cm^{-1} were assigned to P–O stretching mode, whereas the peaks at 561 and 602 cm^{-1} were assigned to the bending vibration mode of the O–P–O bond. The vibration mode of OH^- caused the absorption peak at 631 cm^{-1}. The broad band between 3250 and 3650 cm^{-1} hid the weak OH band at 3572 cm^{-1}. The adsorbed H_2O

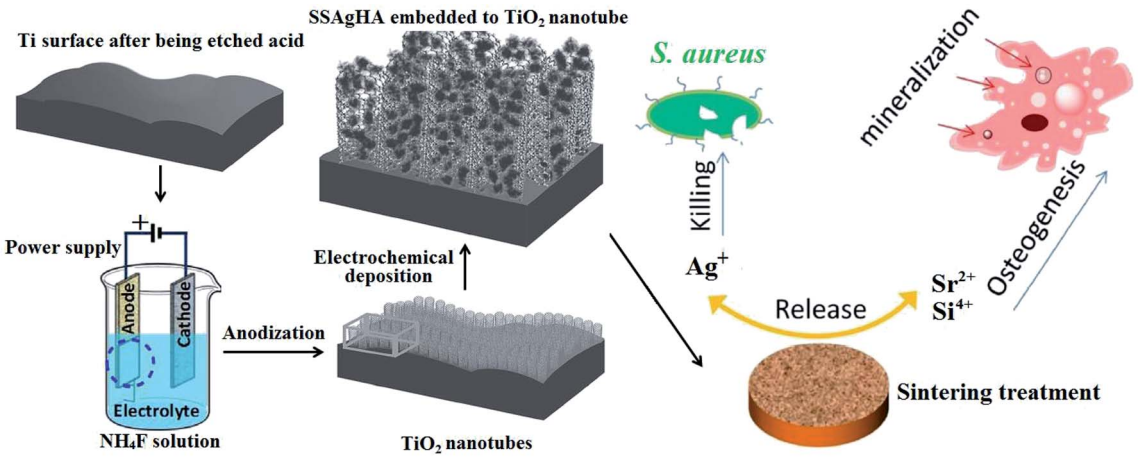

Fig. 1 Schematic of Si/Sr/Ag co-doped HA/TiO_2 nanotube coatings with antibacterial activity and cytocompatibility, which were fabricated by electrodeposition combined with anodization.

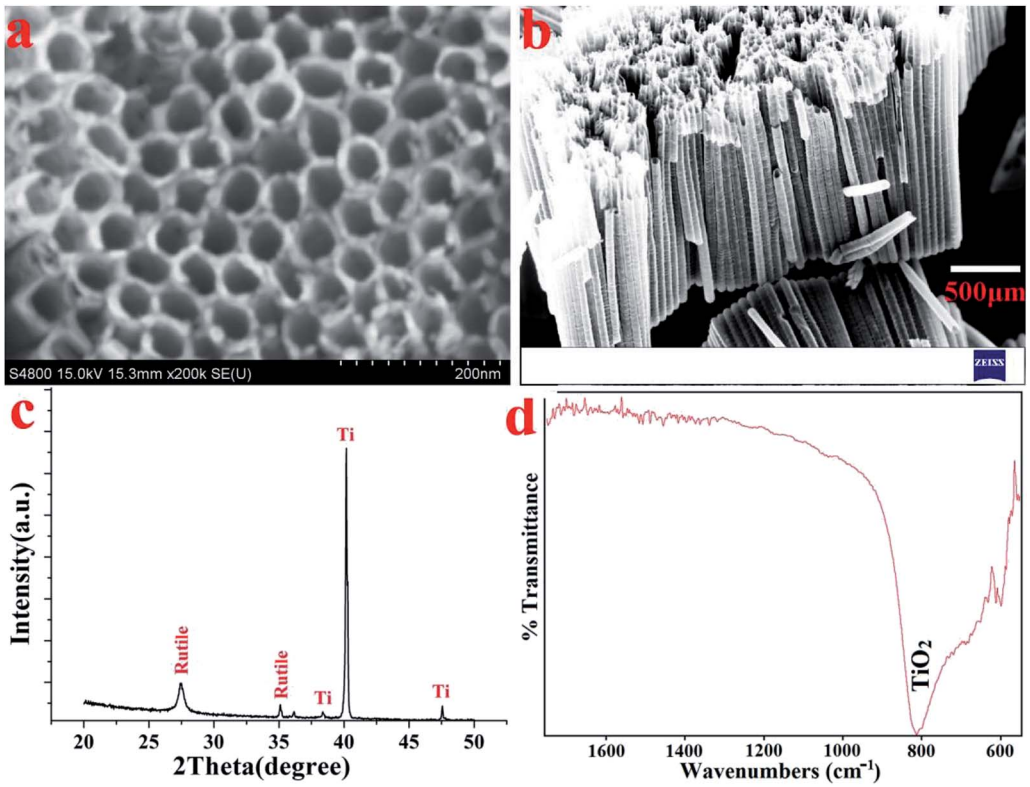

Fig. 2 (a) FE-SEM image, (b) their cross-section, (c) XRD pattern and (d) FT-IR spectra of the anodized and hydrothermally treated Ti substrate.

molecules were responsible for the broad (weak) band that expanded from 3600 cm^{-1} to 3400 cm^{-1} and for the bending peak at 1620 cm^{-1}.[18,38] These peaks were characteristic of HA.

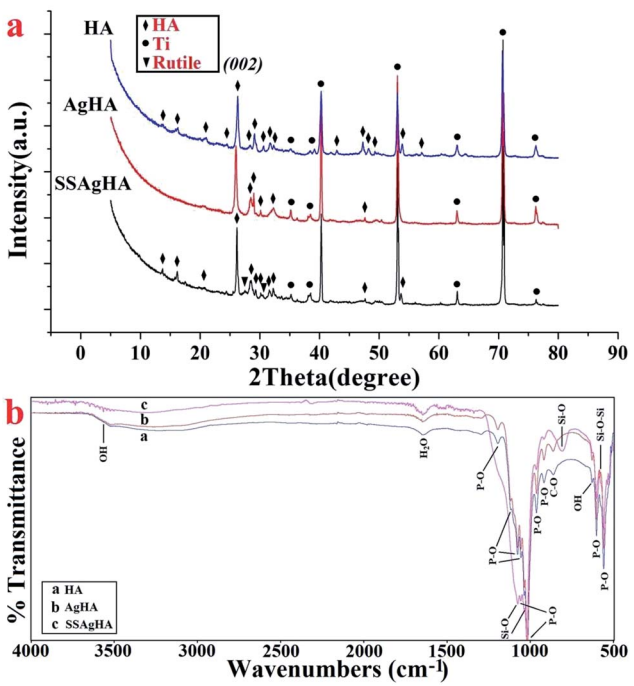

Fig. 3 XRD pattern (a) and FT-IR spectra (b) of the HA, AgHA and SSAgHA/TNT coatings that were deposited on their underlying Ti substrates.

Small peaks at 875 cm^{-1} were related to [CO_3] groups,[18,39] whereas the peak at 875 cm^{-1} may be attributed to HPO_4^{2-} groups.[18,40] However, the peak at 875 cm^{-1} was more likely due to CO_3^{2-} groups, because no other HPO_4^{2-} species were detected. Compared with HA, the bending motion of oxygen atoms along the bisection of the Si–O bending modes of the SiO_4^{2-} group led to the bands at 805 and 1098 cm^{-1}.[41] The band at 571 cm^{-1} resulted from the vibrational bending mode of Si–O–Si.[42] In particular, the absence of any carbonate peak may be due to the replacement of the PO_4^{3-} groups with SiO_4^{2-} rather than CO_3^{2-}.[35] Overall, the FTIR patterns of the HA, AgHA and SSAgHA coatings were similar. These patterns indicated that the asymmetric vibration modes of the main functional groups (PO_4^{3-}, OH^-) were not changed by the incorporation of Ag, Si and Sr into the HA lattice. This conclusion was in agreement with the XRD results given in Fig. 3a.

The overall similarity and closeness of the spectral characteristics of Ag, Ag^+ and Ag^{2+} make it difficult to differentiate them from one another, but some subtle features can separate them.[43] Fig. 4 displays the elemental composition and chemical states of the SSAgHA coating along with the high-resolution XPS spectra of the Ag 3d, Si 2p and Sr 3d regions. The main peaks in the wide-scan XPS spectrum were due to Si, Sr, Ag, Ca and P atoms. The absence of the C 1s peak at 282.4 eV confirmed that carbon was not present in the heat-treated structure of the SSAgHA coating.[43] Narrow-scan XPS analysis revealed detailed information on Si, Sr and Ag in the coating. The Sr 3d spectrum consisted of the Sr 3d5/2 (26.6 eV) and Sr 3d3/2 (26.6 eV) photoelectron lines (Fig. 4d), which showed the typical Sr

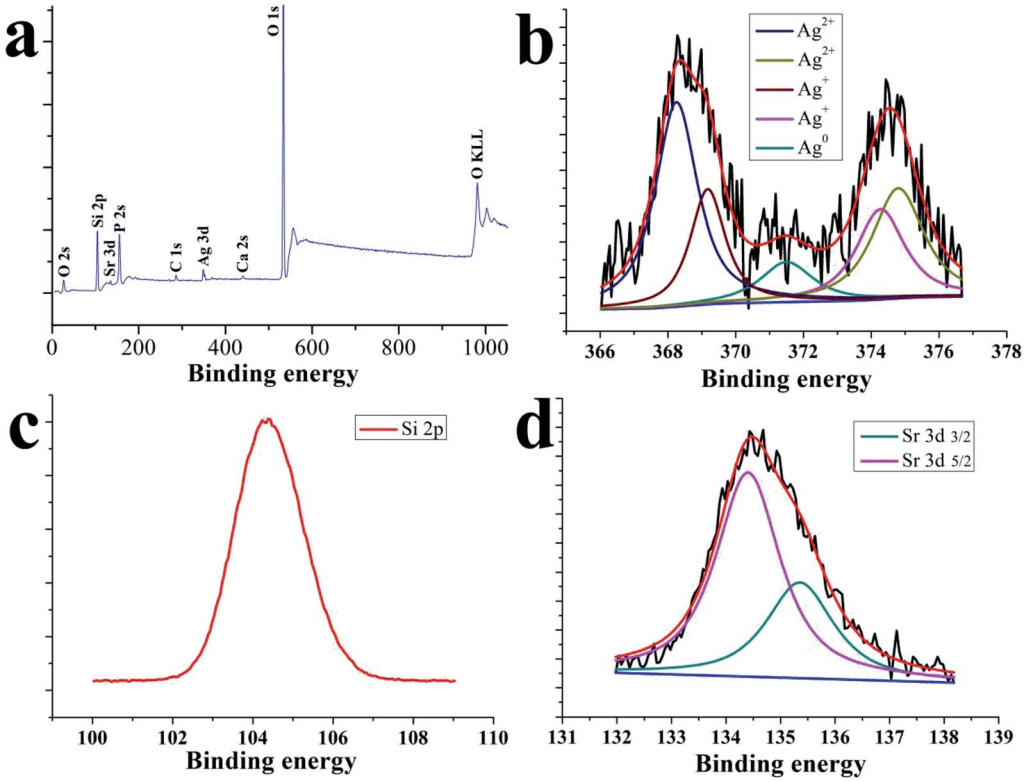

Fig. 4 XPS general spectrum of the surface of the SSAgHA/TNT coating.

chemical bonding states in the SSAgHA coating. The narrow-scan given in Fig. 2b showed the Ag 3d5/2 and Ag 3d3/2 peaks at 368.0 and 374.0 eV, respectively; their difference of 5.9 reflected the metallic state in the coating.[43] Besides, the O 1s spectrum had a binding energy of 529.7 eV. The shoulder extending from 530 eV to 532.5 eV indicated that oxygen was present in other chemical states, such as adsorbed water, silver carbonate and bicarbonate, as well as an oxygen-containing C species. These results were consistent with previously published XPS data for SrAgHA or SiAgHA.[35,44]

The FESEM views from the top surfaces of the HA and AgHA coatings in Fig. 5a and b suggested that both coatings exhibited similar dense microstructural features, such as needle-like crystals. However, the AgHA crystals appeared to be relatively finer than the HA crystals, which had a denser fibrous structure. These morphologies were consistent with our previous findings.[45] The SEM images in Fig. 5c indicated that the SSAgHA/TNT composite coating possessed 3D interconnected macropores. The sizes of the macropores in the composite coating were mainly distributed around 10–20 μm. Fig. 5d–i show representative images of the surface roughness and hydrophilicity tests. The roughest surface amongst the samples was that of SSAgHA with a roughness value of 1.23 μm, which was due to its reticulated porous morphology. A rough surface provides additional binding sites for proteins, thereby enhancing cell attachment and proliferation. Osteoblast cells respond well to a rough surface.[46–49] The surface topography can significantly influence the adsorption of extracellular matrix (ECM) proteins,[47,50] whose interactions with cells initiate the cellular response to biomaterials.[51] By favouring protein adsorption, surface wettability can also considerably impact cell adhesion/activation.[52] HA and AgHA surfaces are rather hydrophilic with water contact angles of about 15.5° and 9.1°, respectively. Notably, the SSAgHA coating showed total hydrophilicity, because its water contact angle could not be measured. The roughness of a flat surface with a contact angle less than 90° can affect its wettability.[53,54] The larger the surface roughness is, the better the surface wettability will be. This relationship significantly influences cell activity and may greatly affect the osteoinductive properties of biomaterials.

EDS analysis confirmed the chemical composition of HA, AgHA and Sr/Si-doped AgHA. Fig. 6b reveals the existence of elements, such as P, Ca, Ag and O, in AgHA. Fig. 6c confirms the presence of Sr, Ag, Ca, P, Si and O elements in SSAgHA, and this result was in agreement with the XPS survey scan in Fig. 4a. Ca and P were mainly from HA, and Ti was from the underlying Ti substrate. The Sr, Ag and Si elements were strategically incorporated into the structure of the synthetic HA. The corresponding EDS mapping reflected the uniform distribution of the Sr, Ag, Ca, P and Si elements across the surface of the SSAgHA composite coating (Fig. 6d).

The cross-section views of the double-layer SSAgHA/TNT coating in Fig. 7a indicated that the double-layer coating was composed of an inner compact layer (TNT) and an outer apatite layer. The thicknesses of the inner and outer layers were about 2 and 10 μm, respectively. No apparent discontinuity between the outer and inner layers of the composite coating was observed, but the side surface of the coated sample was severely ground

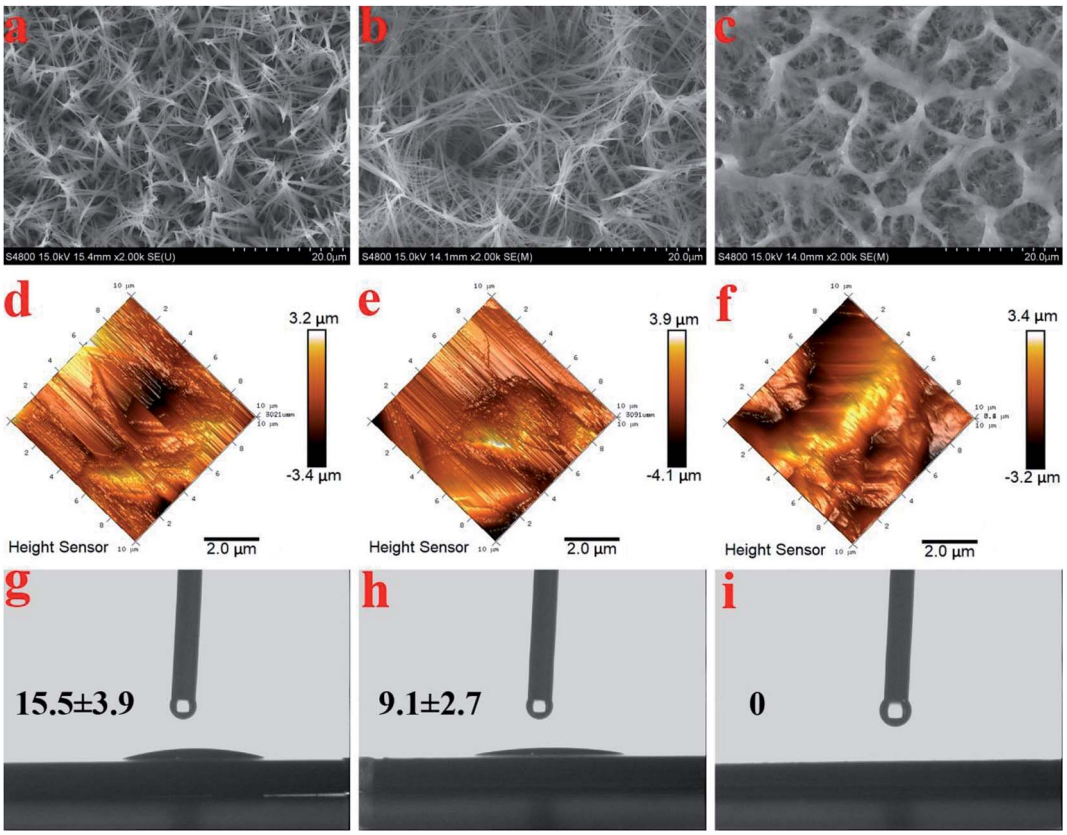

Fig. 5 SEM images of the HA, AgHA and SSAgHA/TNT coatings (a–c); their AFM images (d–f); and the images of the water droplet and its corresponding contact angles on the surfaces of the HA, AgHA and SSAgHA/TNT coatings (g–i).

prior to the FE-SEM measurements. The homogeneity and uniformity of the thickness of the composite coating in its different parts are inferred from the elemental mappings of the outer surface of the coating to its inner TNT layer. Such uniform thickness can result in uniform corrosion behaviour of the sample in physiological environments.

The HA/Ti bonding strength was 7.9 ± 3.3 MPa. The bonding strength between the nanotube layer and SSAgHA coating in the SSAgHA/TNT-coated Ti substrate was measured to be 16.9 ± 3.1 MPa, which was higher than the 15 MPa set in the ISO standard 13 779–4:2002 for surgery apatite-coated implants.[55] The rough interface of SSAgHA and TNT translated into high cohesion strength of the SSAgHA layer with the TNT layer[56] and into their mechanical interlocking.[57]

3.3 Ion release profile

Fig. 8 shows the releasing processes of Ca, Ag, Sr and Si ions from the surface of AgHA and SSAgHA after being immersed in PBS solution for different durations. The doses of the released Ca, Ag, Sr and Si ions increased commensurate with the soaking duration; thus, the ions were released constantly. The released Ag^+ ions near the implants can greatly lower the risk of bacterial infection.[58] For the AgHA and SSAgHA samples, the cumulative release profile of Ag^+ ions (Fig. 8b) suggested a two-phase release behaviour from the SSAgHA coating. In the initial 5 days, the surface diffusion of Ag^+ ions led to fast ion release. Subsequently, the slow diffusion of ions from the inner parts of the SSAgHA coating reduced the release rate to 6–14 days. Notably, the first 2 weeks after surgery is the time when infections usually happen.[59] For the SSAgHA sample, the cumulative concentration of Ag^+ ions after 14 days became constant at 0.529 mg L^{-1}, which was about the amount of Ag^+ that a hybrid coating layer of lysozyme, chitosan, HA and Ag on a Ti substrate releases (approximately 0.6 μg mL^{-1});[60] the lysozyme layer lowers the release of Ag^+ ions into the surroundings. Ag release from Ag-containing antimicrobial composites is similar.[61,62] When HA or brushite cement is physically mixed in $AgNO_3$ solution, Ag^+ ions are released rapidly, and their concentrations reach 200 μg L^{-1} after 7 days of immersion in PBS.[61] By contrast, a plasma-sprayed HA/Ag composite coating releases ions with a concentration larger than 300 μg L^{-1} after immersion for 14 days.[62] Ag ions with large concentrations can fight well against bacteria, but such high concentrations may also cause cytotoxicity.[11,15] Moreover, the cumulative concentration of Ag^+ ions released from AgHA after 14 days became constant at 0.711 mg L^{-1}, which was considerably larger than that of SSAgHA. Such high levels of silver release may cause cytotoxicity.

The ion release profile provides us with general information on elements available for cellular activities. Compared with Ag^+, the release of Sr^{2+} or Si^{4+} ions from the SSAgHA coating was slowly sustained at high concentrations; that is, after 14 days, the coating remained immersed in PBS solution, and the Sr^{2+} and Si^{4+} concentrations reached 1.24 and 74 mg L^{-1},

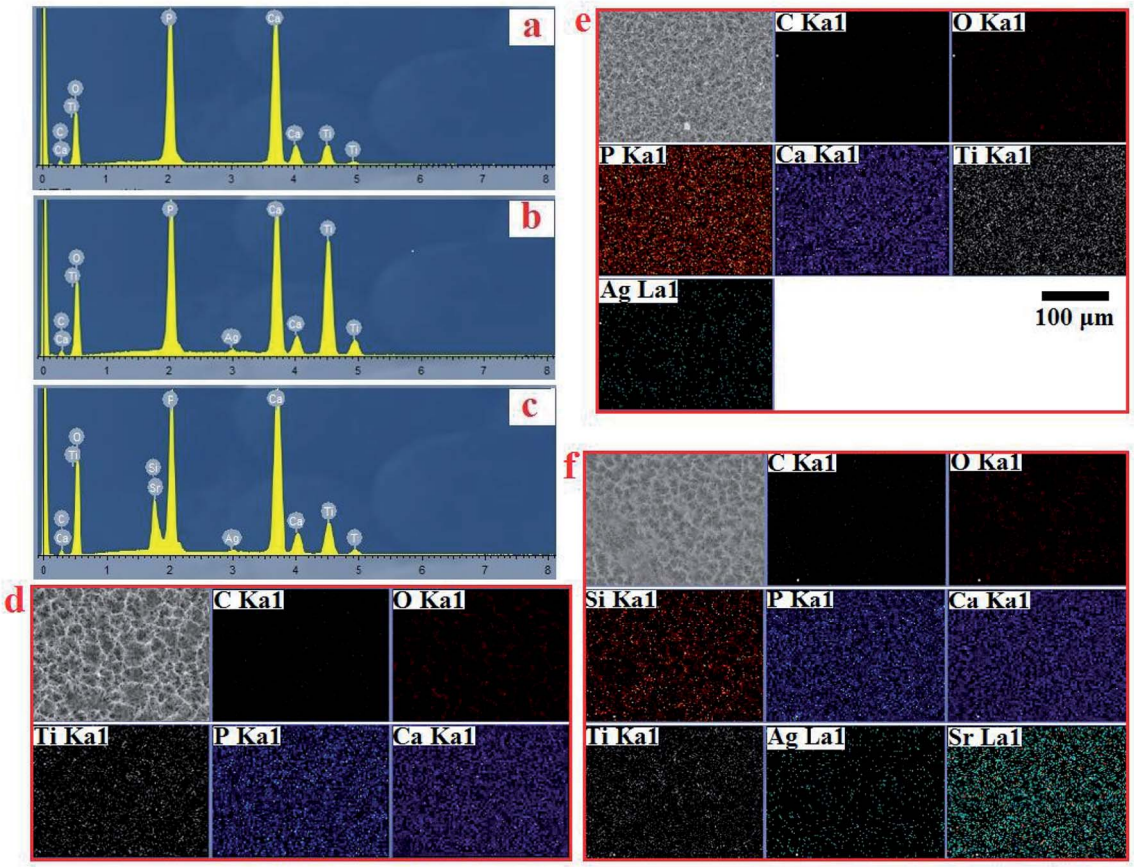

Fig. 6 EDS spectrum of HA, AgHA and SSAgHA/TNT coatings (a–c) and their EDS mapping of HA, AgHA and SSAgHA/TNT coatings (d–f).

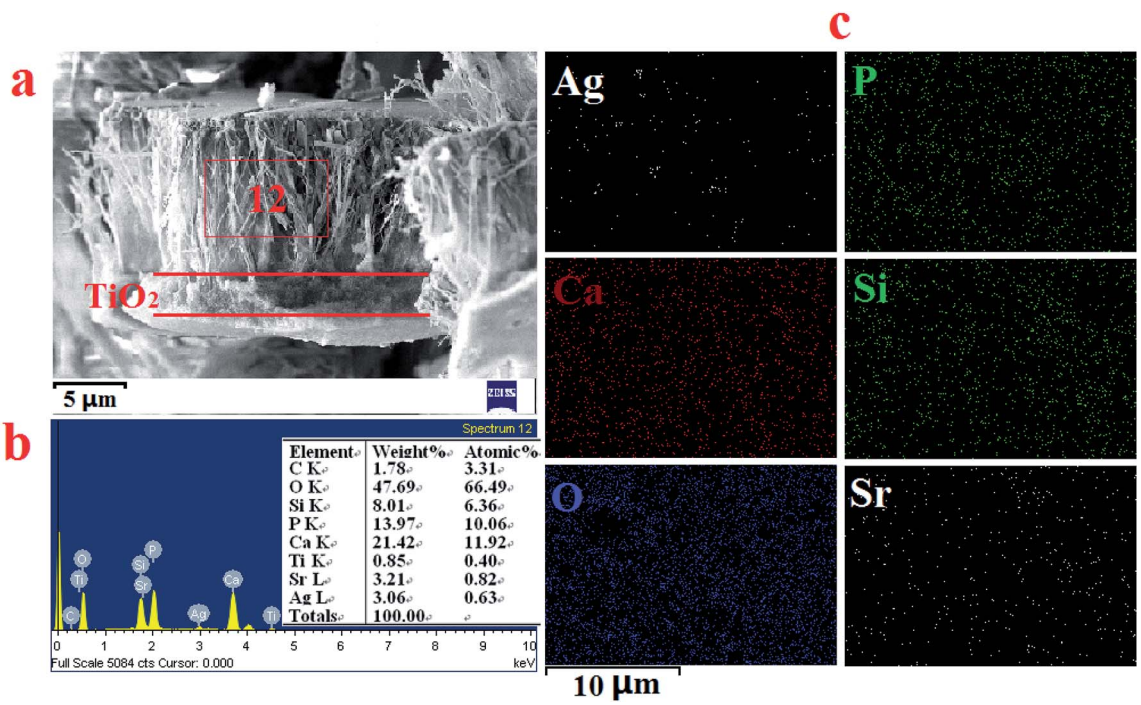

Fig. 7 Cross-section SEM micrographs of the SSAgHA/TNT double coating (a); the EDS spectrum (b) and EDS mapping spectrum (c) of the cross-section SEM micrographs of the SSAgHA/TNT double coating.

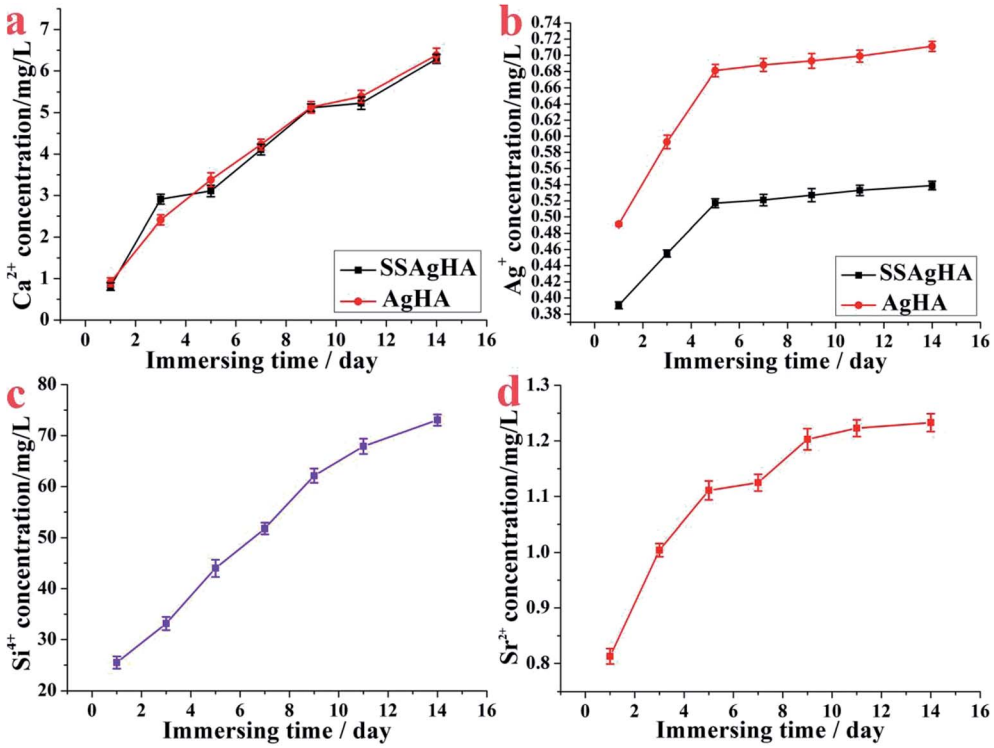

Fig. 8 Amounts of delivered Ca^{2+}, Ag^{+}, Sr^{2+} and Si^{4+} species per surface area released from the SSAgHA/TNT coating under static incubation at 37 °C in PBS.

respectively (Fig. 8c and d). Such relatively high levels of Sr^{2+} and Si^{4+} ions provided bone cells with a readily available pool of essential ions as co-factors during bone regeneration, which considerably increased the osteogenic potential of the material.[19,20] For Ca^{2+} ions, AgHA and SSAgHA samples exhibited similar ion release curves, thereby providing osteogenic mineralisation factors (Fig. 8a).[12]

3.4 Electrochemical studies

To establish the standard OCP in SBF solution, the bare and coated samples were given a sufficient time frame of 1 h. As shown in Fig. 9a, the steady-state potential of the coated sample positively shifted with respect to the bare Ti sample, indicating a decreased corrosion drive; the Cp-Ti, HA, AgHA and SSAgHA samples attained stability with −0.425, −0.345, −0.375 and −0.395 V, respectively. The electrochemical impedance results are expressed in terms of Nyquist plots in Fig. 9b. Except for the linear plot of the HA sample, the plots of the other samples were clearly arc shaped. A high arc depth denotes a high corrosion resistance. The area under curve of the Nyquist phase angle was high for the SSAgHA sample, indicating the capacitive nature of the surface layer to the surrounding electrolyte. The high resistances of the HA and SSAgHA coatings were due to an electrochemically-formed apatite layer and the double-layer of the SSAgHA/TNT coating, respectively.

Fig. 9a shows the potentiodynamic polarisation curves and their corresponding corrosion data. The corrosion potential values of the coated samples gained a positive shift with respect to the bare sample. The corrosion current density of the bare sample was the highest amongst the samples, and this result further confirmed its inferior corrosion resistance before being coated.[63] The improvement in the corrosion resistance of the Ti sample after the application of the SSAgHA/TNT coating may be due to two main reasons. Firstly, the presence of a micron-thick TNT sublayer in the bilayered SSAgHA/TNT coating prevents the corrosive solution from further penetrating through the coating towards the underlying substrate even if microstructural imperfections, such as cracks and pores at the outer surface of the coating, can channel the corrosive ions into the underlying substrate. Secondly, the strong bonding between the underlying Ti substrate and coating makes it stable in a physiological environment, which consequently protects the underlying Ti substrate from the environment.[29]

3.5 *In vitro* antibacterial activity evaluation

The antibacterial activities of HA, AgHA, SrAgHA and SSAgHA against *S. aureus*, the most common infection-causing microorganism, were evaluated *via* the disk diffusion method.[65] Fig. 10e shows the inhibition zones of various coatings towards the strains. Pure HA exhibited no inhibition zone, indicating its poor antibacterial activity against the pathogen. The Ag-doped apatite (AgHA, SrAgHA and SSAgHA) showed excellent inhibition zones for *S. aureus* microorganisms; such zones were found to be similar. To assess antibacterial ability further, we removed the adhered bacteria from the coatings and cultured them on agar plates *via* the bacterial counting method. The results are

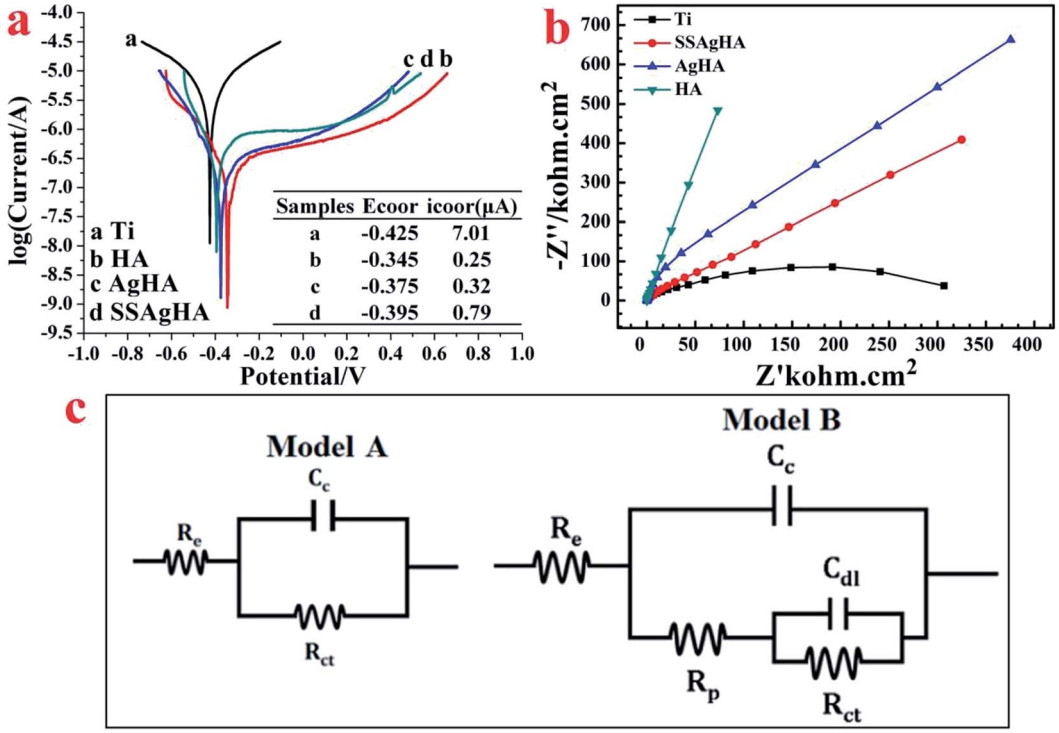

Fig. 9 (a) Tafel polarisation curves of the bare Ti substrate and bioceramic-coated Ti substrate; (b) the Nyquist plots of the bare Ti substrate and bioceramic-coated Ti substrate; (c) the equivalent electrical circuit for fitting the EIS data for the bare Ti substrate and bioceramic-coated Ti substrate.

shown in Fig. 9a–d. The amounts of bacteria on AgHA, SrAgHA and SSAgHA decreased by approximately 100%, 99.2% and 99.5%, respectively (Fig. 10f). These findings supported the excellent antibacterial ability of the Ag-incorporated coatings. The most crucial disinfection mechanism of Ag^{+} ions is to rupture the cell membrane, which then results in the leakage of

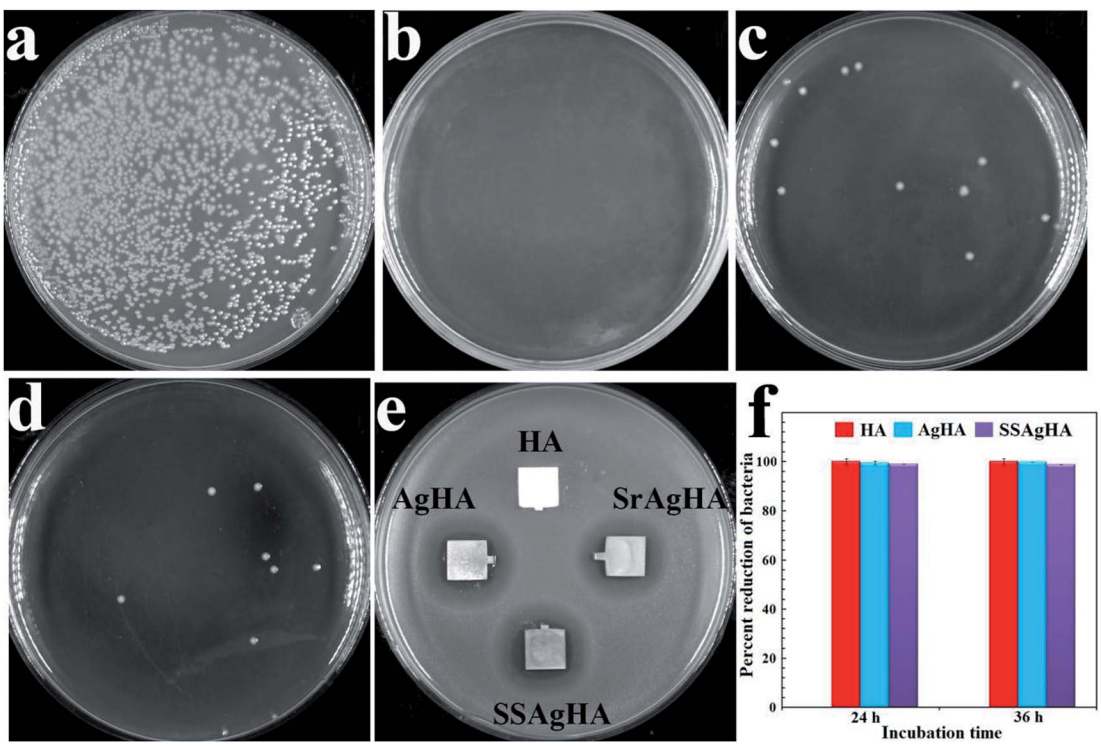

Fig. 10 Representative macroscopic photos of viable adherent *S. aureus* on different surfaces: (a) HA; (b) AgHA; (c) SrAgHA; and (d) SSAgHA. (f) Antimicrobial rates of SSAgHA. (e) The results of the test for the zone of inhibition of HA, AgHA, SrAgHA and SSAgHA against *S. aureus*.

intracellular substances.[66] Intracellular radical oxygen species can also be produced when Ag^+ ions released from the AgHA diffuse into the bacterial cells.[60,67] Bacterial proliferation can be suppressed[60] when the cell-penetrated Ag^+ ions directly interact with phosphorus- and sulphur-containing components, such as DNA, RNA and enzymes.[67]

The amount of Ag^+ ions released from Ag-loaded coatings should be optimal that it trades off high-concentration toxicity for low-concentration ineffectiveness against bacteria.[68,69] Fig. 13b proves the toxicity of the AgHA coating and the non-toxicity of the SSAgHA coating towards the MC3T3-E1s. After SSAgHA was soaked for 14 days, the concentration of its released Ag^+ ions reached 0.525 mg L^{-1} (Fig. 8b). The incorporated Sr and Si in the ASSAgHA coating offset the cytotoxicity of Ag.[1,22]

3.6 Osteoblast morphology

Coatings for bone tissue engineering should exhibit good biocompatibility.[23] Fig. 11a–c show the morphologies of MC3T3-E1 cultured on the HA, AgHA and SSAgHA coatings for 1 day. The cells grew on all these coatings and demonstrated well-spread morphology, which seemingly met the two criteria required for biocompatibility: chemical inertness and absence of toxicity. However, we evaluated osteoblast viability after 3 days by using live/dead fluorescence staining (Fig. 11d–f). The AgHA coating showed remarkable cytotoxicity, resulting in extensive cell death. The SSAgHA coating did not exhibit any cytotoxic distress due to the presence of strontium and silicon ions.[19,20] Therefore, the HA- and SSAgHA-coated surfaces provided a bio-integrative environment for the attachment, proliferation and differentiation of cells.

The cells were firmly attached to the surfaces of the HA and SSAgHA coatings; their cytoskeletons were elongated, and the morphology of their actin filaments was well spread; Fig. 12 shows the filaments in red, and the cell nuclei in blue.[64] The fluorescence images show normal morphology (Fig. 12). By contrast, the cells on the AgHA coating were not widely spread and small; that is, the formation of actin fibres was less developed. The number of cells on the AgHA coating decreased with high concentrations of Ag, and this result was in line with the findings of live/dead fluorescence staining and Alamar Blue assay after 3 days of culture.

3.7 Osteoblast adhesion and proliferation

Fig. 13a provides further information on the response of osteoblasts on the trace Ag–Si–Sr-co-doped HA coating. The cell amount at 2 h was about twice that at 1 h, although no significant difference was observed amongst the groups ($p > 0.05$).

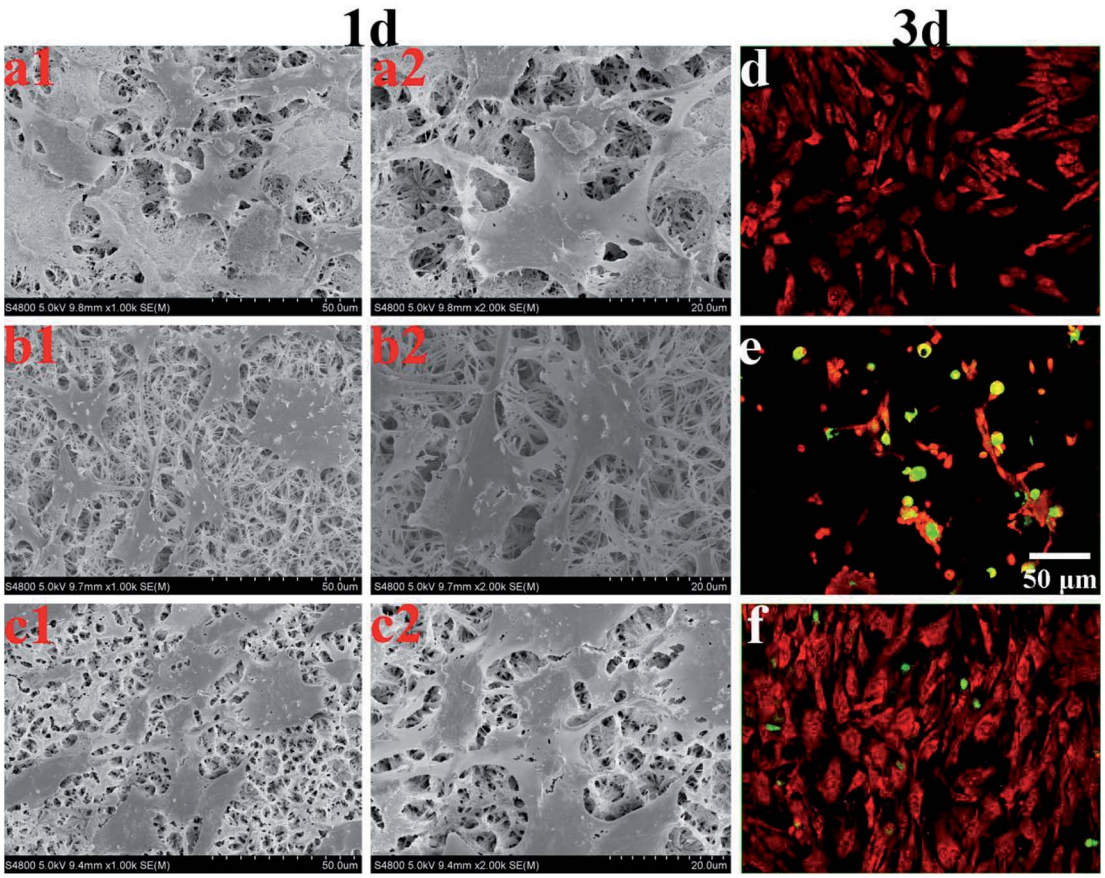

Fig. 11 SEM morphologies of the MC3T3-E1 cells on HA (a), AgHA (b) and SSAgHA/TNT coatings (c) for 1 day; the dead/live staining images of MC3T3-E1 cells cultured on the surfaces of HA (d), AgHA (e) and SSAgHA/TNT (f) coatings for 3 days. Green fluorescence – nuclei of dead cells, red fluorescence – viable cells.

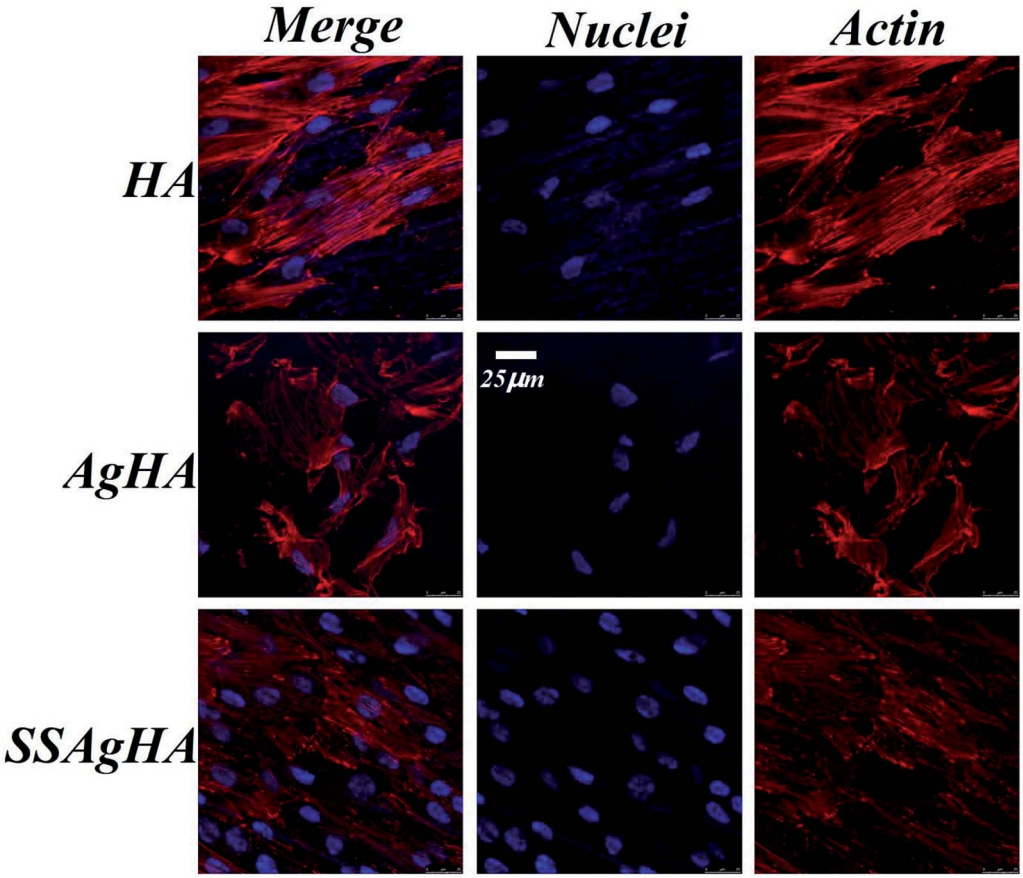

Fig. 12 Laser scanning confocal microscope images of the MC3T3-E1 cells cultured on the surfaces of HA, AgHA and SSAgHA/TNT coatings after 3 days of culture.

The above data demonstrated that all the coatings were not toxic to MC3T3-E1, providing a friendly environment for the cells to adhere and grow.

Fig. 13b shows the continuously increasing proliferation of MC3T3-E1 cells on the surfaces of the HA, AgHA and SSAgHA coatings for an extended culture time. After 7 days of culture, the numbers of cells on the surfaces of all the three coatings were approximately more than three times their corresponding numbers of cells after 1 day of culture. For all the incubation time periods (1, 3 and 7 days), the numbers of adherent cells cultured on the surfaces of the HA and SSAgHA coatings significantly increased compared with the number of cells cultured on the surface of the AgHA coating ($p < 0.01$). After 1 day of culture, the AgHA coating showed reduced cell viability due to a high cumulative concentration of released Ag^{+}. Such an abrupt release of ions at an early stage of culture, *i.e.* before 7 days, could negatively influence cell viability, which led to a certain degree of cell loss.[11,15,69,70] The cell proliferation of the SSAgHA coating significantly increased compared with that of the HA coating ($p < 0.01$) after 7 days of culture. These results demonstrated that Si–

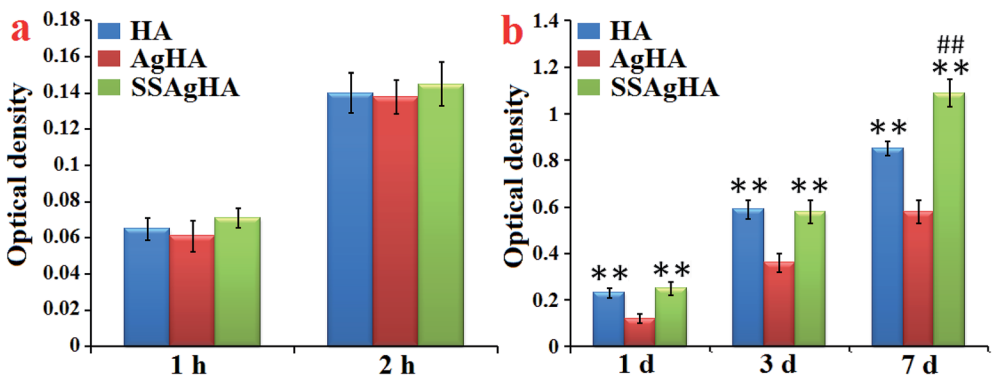

Fig. 13 Osteoblast (a) adhesion and (b) proliferation on the surfaces of HA, AgHA and SSAgHA/TNT coatings. *$p < 0.05$, **$p < 0.01$ compared with AgHA and #$p < 0.05$ and ##$p < 0.01$ compared with HA.

Sr co-doping could effectively promote the proliferation of MC3T3-E1 and successfully offset the potential cytotoxicity of Ag ions. The SEM images (Fig. 11) together with the cell proliferation assay (Fig. 13) demonstrated that the SSAgHA coating was nontoxic to cells and biocompatible for adhesion.

3.8 Osteogenic differentiation

The SSAgHA coating was selected for further tests on osteogenic effects due to its excellent *in vitro* cytocompatibility and antibacterial activity. The osteogenesis-related gene expression levels were examined *via* qRT-PCR (Fig. 14). The osteogenesis-related genes whose expressions could be promoted by the surfaces of the HA and SSAgHA coatings included (i) ALP, an early marker of osteogenic differentiation; (ii) Col-1, which mainly forms the ECM of bone; (iii) bone morphogenetic protein 2; (iv) runt-related transcription factor (RUNX)2 and (v) OCN and OPN, the late markers of osteogenic differentiation. Compared with the bare Ti substrate, the HA and SSAgHA surfaces showed a considerable improvement in osteogenic activity, confirming the negligible effect of Ag^{+} on cell viability. Interestingly, when Sr and Si were incorporated into AgHA, the expression levels of the osteogenesis-related genes were enhanced more significantly than those of the osteoblasts that were grown on the HA coating.[71] As demonstrated in Fig. 13b, after 7 days of culture on the HA surface, osteoblast proliferation was lower than that on the SSAgHA surface after the same time period. This result was in line with the osteoblast differentiation results obtained after 14 days of culture (Fig. 14).

Sr enhances *in vitro* and *in vivo* bone formation,[72] and Si in HA results in efficient osseointegration activities.[73] Therefore, the inducement of bone formation and the reduction in bone resorption can be achieved by delivering multiple ion species from HA, which is attainable by Sr–Si co-doping into AgHA.[74]

The effects of Si and Sr ions on bone-related cells depend on dosage.[19,75] For high biological activity of Si–HA coatings and good adhesion of human osteoblast-like cells to their surfaces, the optimal Si content is 2.2 wt% (13 mol%),[76] which was remarkably lower than the amount of silicon that was incorporated into the SSAgHA coatings synthesised in the present study. In addition, if the growth medium of human osteoblasts is supplemented with 0.03 mmol L^{-1} silicon, then their metabolic activity and proliferation are enhanced.[77] For strontium concentrations lower than 8.3 wt% (10 mol%), Sr–HA coatings can promote the proliferation and differentiation of osteoprecursors and MG63 cells.[20] Braux *et al.* found that the proliferation of human primary bone cells is enhanced in the presence of 0.01–0.1 mmol L^{-1} Sr^{2+} ions.[77] Lower than the amounts we observed in the present study, the concentrations of Si and Sr in normal serum are 2.14×10^{-2} and $1.14–2.48 \times 10^{-3}$ mmol L^{-1}, respectively.[78,79] However, compared with blood, bone tissue contains considerably higher amounts of Si and Sr. The Si content in bones and ligaments is about 100 mg kg^{-1}.[80] Moreover, 99.1% of the absorbed Sr is deposited in bones (36–140 mg kg^{-1}).[81,82] Therefore, a specific high dose of Si and Sr makes osteoprogenitor cells and bone tissues proliferate and regenerate well.[19,83–87]

SSAgHA not only increased cell proliferation and osteogenic-related gene expression levels but also inhibited the growth of *S. aureus* for 7 days. Its biological properties were superior to those of the HA and Ag-HA coatings, and its antibacterial efficacy was comparable with the Ag–HA coating (Fig. 10). The mesoporous channel structures of the SSAgHA coating may be applied to topical drug or gene delivery.[17]

Therefore, the *in vitro* induction of osteogenesis by the SSAgHA extracts could possibly be due to the simultaneous stimulation by Si and Sr ions. Although 8.01 wt% of Si and 3.21 wt% of Si in our investigated SSAgHA coating could

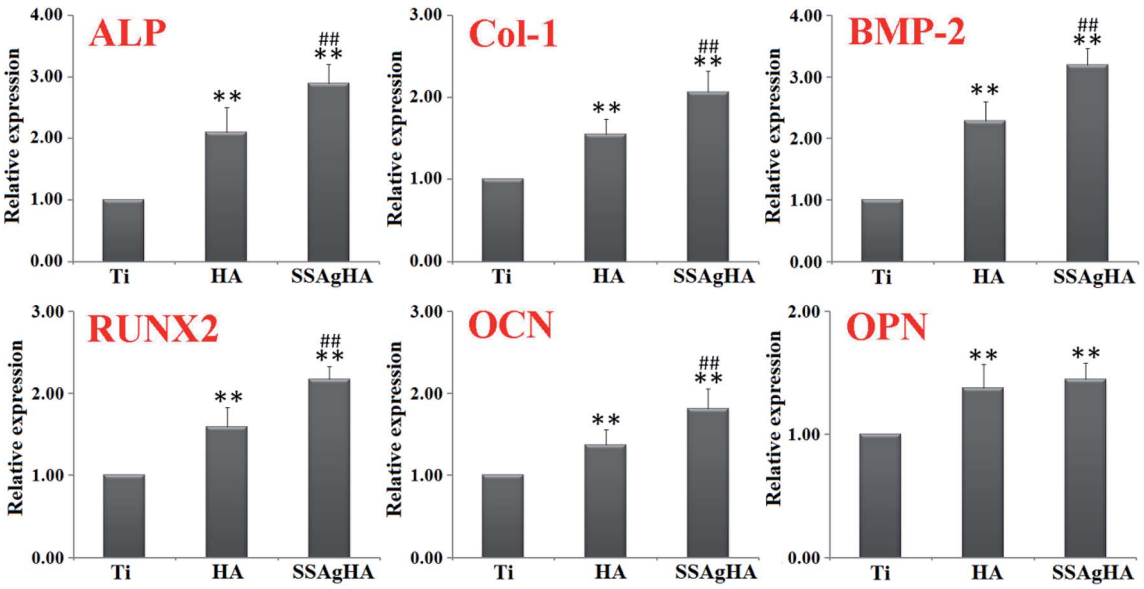

Fig. 14 Relative expression levels of ALP, type-1 collagen (Col-1), bone morphogenetic protein (BMP-2), RUNX2, osteocalcin (OCN) and osteopontin (OPN) in the osteoblasts that were cultured on each sample for 14 days. The values were normalised to the expression level of glyceraldehyde 3-phosphate dehydrogenase (GAPDH). *$p < 0.05$, **$p < 0.01$ compared with Ti and #$p < 0.05$ and ##$p < 0.01$ compared with HA.

improve the bioactivity, their optimum concentrations need to be determined in further studies. Moreover, an understanding of the mechanism by which Si–Sr co-doping of HA promotes osteogenic behaviour warrants further research.

4. Conclusions

For the first time, we fabricated an SSAgHA/TNT bilayer coating that simultaneously exhibited excellent cytocompatibility, osteogenic activity and antibacterial property. The coating possessed 3D interconnected macropores with a pore size of 10–20 μm. The Ag, Sr and Si ions were incorporated uniformly on the surface. The SSAgHA/TNT coating enhanced the corrosion resistance of the bare underlying Ti substrate even though the HA-coated Ti substrate demonstrated the highest electrochemical corrosion resistance. The bonding strength of the fabricated SSAgHA/TNT structure was satisfactory. Results of the *in vitro* experiment revealed that the HA and SSAgHA coatings showed excellent biocompatibility and provided a friendly environment for the adhesion and growth of MC3T3-E1s, but the AgHA coating showed some cytotoxicity. The good osteoinductivity and antibacterial ability of SSAgHA were attributed to the Sr/Si elements and Ag ions, respectively. The released Sr^{2+}/Si^{4+} ions from SSAgHA enhanced cell proliferation, increased the expression levels of osteogenesis-related genes and successfully offset the potential cytotoxicity of Ag ions. They reduced the initial content of Ag to weaken the cytotoxicity of Ag^{+} ions without reducing antibacterial efficacy. In addition, the released Ag^{+} ions from SSAgHA inhibited the growth and attachment of *S. aureus*. In conclusion, the SSAgHA coating exerted two effects on the surface: resisting bacterial adhesion and enhancing cellular interactions at the bio-interface, making it a promising candidate for preventing infections and repairing bone defects.

Conflicts of interest

There are no conflicts to declare.

Acknowledgements

This work was supported by Innovative Talent Support Program of Hebei Province (Hundred people plan), the Second Batch of Young Top-notch Talent Fund of Hebei Province (China), the Science and Technology Research Project of Zhangjiakou (China, 17120012D, 1811033D), the Medical Science Research Planning Project of the Health and Family Planning Commission of Hebei Province (China, 20180810), the Natural Science Foundation of Hebei Province (China, H2016405008), the Youth Fund of Science and Technology of Hebei Colleges (China, QN2017010), the Population Health Information in Hebei Province Engineering Technology Research Center, and the Development Program of the Self-Funded Project of Zhangjiakou City of 2018 (1821119D), College Students Innovation and Entrepreneurship Training Program (201810092003). Moreover, we are grateful to Dr Ali Safaei (from Institute of Nanoparthava) for his technical editing, *i.e.* language and substantive editing, of the manuscript.

References

1 P. N. Lim, T. Konishi, Z. Wang, J. Feng, L. Wang, J. Han, Z. Yang and E. S. Thian, Enhancing osteoconductivity and biocompatibility of silver-substituted apatite in vivo through silicon co-substitution, *Mater. Lett.*, 2018, **212**, 90–93.

2 B. Aksakal, Y. Say, Ç. Buyukpinar and S. Bakirdere, Biodegradation of hydroxyapatite coated Rex-734 alloy with silver and selenium/chitosan substitutions: In vitro analysis, *Ceram. Int.*, 2017, DOI: 10.1016/j.ceramint.2017.06.139.

3 R. Rasouli, A. Barhoum and H. Uludag, A review of nanostructured surfaces and materials for dental implants: surface coating, patterning and functionalization for improved performance, *Biomater. Sci.*, 2018, DOI: 10.1039/c8bm00021b.

4 C. F. Marques, S. Olhero, J. C. C. Abrantes, A. Marote, S. Ferreira, S. I. Vieira and J. M. F. Ferreira, Biocompatibility and antimicrobial activity of biphasic calcium phosphate powders doped with metal ions for regenerative medicine, *Ceram. Int.*, 2017, **43**, 15719–15728.

5 L. Bai, Z. B. Du, J. J. Du, W. Yao, J. M. Zhang, Z. M. Weng, S. Liu, Y. Zhao, Y. L. Liu, X. Y. Zhang, X. B. Huang, X. H. Yao, R. Crawford, R. Q. Hang, D. Huang, B. Tang and Y. Xiao, A multifaceted coating on titanium dictates osteoimmunomodulation and osteo/angiogenesis towards ameliorative osseointegration, *Biomaterials*, 2018, DOI: 10.1016/j.biomaterials.2018.02.010.

6 F. Qu, T. Zhang, H. W. Gu, Q. Q. Qiu, F. Z. Ding, X. Y. Peng and H. Y. Wang, Electrical and Optical Properties of ZnO: Al Films with Different Hydrogen Contents in Sputtering Gas, *Rare Met.*, 2015, **34**, 173–177.

7 P. Li, Y. F. Poon, W. Li, H. Y. Zhu, S. H. Yeap, Y. Cao, X. Qi, C. Zhou, M. Lamrani, R. W. Beuerman, E. T. Kang, Y. Mu, C. M. Li, M. W. Chang, S. S. Leong and M. B. A. Chan-Park, Polycationic Antimicrobial and Biocompatible Hydrogel with Microbe Membrane Suctioning Ability, *Nat. Mater.*, 2011, **10**, 149–156.

8 L. Zhang, C. Ning, T. Zhou, X. Liu, K. W. Yeung, T. Zhang, Z. Xu, X. Wang, S. Wu and P. K. Chu, Polymeric Nanoarchitectures on Ti-Based Implants for Antibacterial Applications, *ACS Appl. Mater. Interfaces*, 2014, **6**, 17323–17345.

9 T. Wang, X. Liu, Y. Zhu, Z. D. Cui, X. J. Yang, H. Pan, K. W. K. Yeung and S. Wu, Metal Ion Coordination Polymer-Capped pH-Triggered Drug Release System on Titania Nanotubes for Enhancing Self-Antibacterial Capability of Ti Implants, *ACS Biomater. Sci. Eng.*, 2017, **3**, 816–825.

10 S. Lin, X. Liu, L. Tan, Z. Cui, X. Yang, K. W. K. Yeung, H. Pan and S. Wu, Porous Iron-Carboxylate Metal-Organic Framework: A Novel Bioplatform with Sustained Antibacterial Efficacy and Nontoxicity, *ACS Appl. Mater. Interfaces*, 2017, **9**, 19248–19257.

11 A. Nel, T. Xia, L. Madler and N. Li, Toxic Potential of Materials at the Nanolevel, *Science*, 2006, **311**, 622–627.

12 Y. Z. Zhang, X. M. Liu, Z. Y. Li, S. L. Zhu, X. B. Yuan, Z. D. Cui, X. J. Yang, P. K. Chu and S. L. Wu, Nano Ag/ZnO

Incorporated Hydroxyapatite Composite Coatings: Highly Effective Infection Prevention and Excellent Osteointegration, *ACS Appl. Mater. Interfaces*, 2018, DOI: 10.1021/acsami.7b17351.

13 H. Qin, H. Cao, Y. Zhao, C. Zhu, T. Cheng, Q. Wang, X. Peng, M. Cheng, J. Wang, G. Jin, Y. Jiang, X. Zhang, X. Liu and P. K. Chu, In Vitro and in Vivo Anti-Biofilm Effects of Silver Nanoparticles Immobilized on Titanium, *Biomaterials*, 2014, **35**, 9114–9125.

14 X. Xie, C. Mao, X. Liu, Y. Zhang, Z. Cui, X. Yang, K. W. K. Yeung, H. Pan, P. K. Chu and S. Wu, Synergistic Bacteria Killing through Photodynamic and Physical Actions of Graphene Oxide/Ag/Collagen Coating, *ACS Appl. Mater. Interfaces*, 2017, **9**, 26417–26428.

15 G. Veronesi, C. Aude-Garcia, I. Kieffer, T. Gallon, P. Delangle, N. Herlin-Boime, T. Rabilloud and M. Carriere, Exposure-Dependent Ag^+ Release from Silver Nanoparticles and its Complexation in AgS_2 Sites in Primary Murine Macrophages, *Nanoscale*, 2015, **7**, 7323–7330.

16 W. S. W. Harun, R. I. M. Asri, J. Alias, F. H. Zulkifli, K. Kadirgama, S. A. C. Ghani and J. H. M. Shariffuddin, A comprehensive review of hydroxyapatite-based coatings adhesion on metallic biomaterials, *Ceram. Int.*, 2017, DOI: 10.1016/j.ceramint.2017.10.162.

17 D. F. Silva, T. E. Friis, N. H. A. Camargo and Y. Xiao, Characterization of mesoporous calcium phosphates from calcareous marine sediments containing Si, Sr and Zn for bone tissue engineering, *J. Mater. Chem. B*, 2016, **4**, 6842–6855.

18 L. Robinson, K. Salma-Ancane, L. Stipniece, B. J. Meenan and A. R. Boyd, The deposition of strontium and zinc Co-substituted hydroxyapatite coatings, *J. Mater. Sci.: Mater. Med.*, 2017, **28**, 51–63.

19 K. L. Lin, X. H. Wang, N. Zhang and Y. H. Shen, Strontium (Sr) strengthens the silicon (Si) upon osteoblast proliferation, osteogenic differentiation and angiogenic factor expression, *J. Mater. Chem. B*, 2016, **4**, 3632–3638.

20 J. Y. Gao, M. Wang, C. Shi, L. P. Wang, D. L. Wang and Y. C. Zhu, Synthesis of trace element Si and Sr codoping hydroxyapatite with non-cytotoxicity and enhanced cell proliferation and differentiation, *Biol. Trace Elem. Res.*, 2016, **174**, 208–217.

21 L. Casarrubios, M. C. Matesanz, S. Sánchez-Salcedo, D. Arcos, M. Vallet-Regí and M. T. Portolés, Nanocrystallinity effects on osteoblast and osteoclast response to silicon substituted hydroxyapatite, *J. Colloid Interface Sci.*, 2016, **582**, 112–120.

22 D. Cao, Z. Xu, Y. Chen, Q. Ke, C. Zhang and Y. Guo, Ag-loaded MgSrFe-layered double hydroxide/chitosan composite scaffold with enhanced osteogenic and antibacterial property for bone engineering tissue, *J. Biomed. Mater. Res., Part B*, 2017, DOI: 10.1002/jbm.b.33900.

23 Z. L. Xu, Y. Lei, W. J. Yin, Y. X. Chen, Q. F. Ke, Y. P. Guo and C. Q. Zhang, Enhanced antibacterial activity and osteoinductivity of Ag-loaded strontium hydroxyapatite/chitosan porous scaffolds for bone tissue engineering, *J. Mater. Chem. B*, 2016, **4**, 7919–7928.

24 A. Singh, G. Singh and V. Chawla, Characterization and Mechanical Behavior of Reinforced Hydroxyapatite Coatings Deposited by Vacuum Plasma Spray on SS-316L Alloy, *J. Mech. Behav. Biomed. Mater.*, 2018, DOI: 10.1016/j.jmbbm.2018.01.005.

25 D. M. Liu, Q. Yang and T. Troczynski, Sol-gel hydroxyapatite coatings on stainless steel substrates, *Biomaterials*, 2002, **23**, 691–698.

26 G. P. Dinda, J. Shin and J. Mazumder, Pulsed laser deposition of hydroxyapatite thin films on Ti-6Al-4V: effect of heat treatment on structure and properties, *Acta Biomater.*, 2009, **5**, 1821–1830.

27 A. Vladescu, C. M. Cotrut, F. A. Azem, M. Bramowicz, I. Pana, V. Braic, I. Birlik, A. Kiss, M. Braic, R. Abdulgader, R. Booysen, S. Kulesza and T. K. Monsees, Sputtered Si and Mg doped hydroxyapatite for biomedical applications, *Biomed. Mater.*, 2018, **13**, 025011.

28 M. Javidi, S. Javadpour, M. E. Bahrololoom and J. Ma, Electrophoretic deposition of natural hydroxyapatite on medical grade 316L stainless steel, *Mater. Sci. Eng., C*, 2008, **28**, 1509–1515.

29 L. Fathyunes and J. Khalil-Allafi, The effect of graphene oxide on surface features, biological performance and bio-stability of calcium phosphate coating applied by pulse electrochemical deposition, *Appl. Surf. Sci.*, 2018, **437**, 122–135.

30 Y. L. Lai, P. Y. Cheng, C. C. Yang and S. K. Yen, Electrolytic deposition of hydroxyapatite/calcium phosphate-heparin/gelatin-heparin tri-layer composites on NiTi alloy to enhance drug loading and prolong releasing for biomedical applications, *Thin Solid Films*, 2018, **649**, 192–201.

31 Y. Huang, W. D. Wang, X. J. Zhang, X. T. Liu, Z. W. Xu, S. G. Han, Z. B. Su, H. Y. Liu, Y. Gao and H. J. Yang, A prospective material for orthopedic applications: Ti substrates coated with a composite coating of a titania-nanotubes layer and a silver-manganese doped hydroxyapatite layer, *Ceram. Int.*, 2018, **44**, 5528–5542.

32 Z. Mao, Y. Li, Y. Yang, Z. Fang, X. Chen, Y. Wang, J. Kang, X. Qu, W. Yuan, K. Dai and B. Yue, Osteoinductivity and Antibacterial Properties of Strontium Ranelate-Loaded Poly(Lactic-co-Glycolic Acid) Microspheres With Assembled Silver and Hydroxyapatite Nanoparticles, *Front. Pharmacol.*, 2018, DOI: 10.3389/fphar.2018.00368.

33 H. X. Qiao, Q. S. Zou, C. F. Yuan, X. J. Zhang, S. G. Han, Z. H. Wang, X. P. Bu, H. Tang and Y. Huang, Composite coatings of lanthanum-doped fluor-hydroxyapatite and a layer of strontium titanate nanotubes: fabrication, bio-corrosion resistance, cytocompatibility and osteogenic differentiation, *Ceram. Int.*, 2018, **44**, 16632–16646.

34 Y. Huang, G. Q. Song, X. T. Chang, Z. H. Wang, X. J. Zhang, S. G. Han, Z. B. Su, H. J. Yang, D. D. Yang and X. J. Zhang, Nanostructured Ag^+-substituted fluorhydroxyapatite-TiO_2 coatings for enhanced bactericidal effects and osteoinductivity of Ti for biomedical applications, *Int. J. Nanomed.*, 2018, **13**, 2665–2684.

35 Y. Huang, Z. W. Xu, X. J. Zhang, X. T. Chang, X. Y. Zhang, Y. C. Li, T. Ye, R. Han, S. G. Han, Y. Gao, X. Du and H. J. Yang, Nanotube-formed Ti substrates coated with silicate/silver co-doped hydroxyapatite as prospective materials for bone implants, *J. Alloys Compd.*, 2017, **697**, 182–199.

36 Y. Parcharoen, P. Kajitvichyanukul, S. Sirivisoot and P. Termsuksawad, Hydroxyapatite electrodeposition on anodized titanium nanotubes for orthopedic applications, *Appl. Surf. Sci.*, 2014, **311**, 54–61.

37 K. Lee, Y. H. Jeong, W. A. Brantley and H. C. Choe, Surface characteristics of hydroxyapatite films deposited on anodized titanium by an electrochemical method, *Thin Solid Films*, 2013, **546**, 185–188.

38 D. Gopi, S. Ramyaa, D. Rajeswaria, P. Karthikeyana and L. Kavitha, Strontium, cerium co-substituted hydroxyapatite nanoparticles: synthesis, characterization, antibacterial activity towards prokaryotic strains and in vitro studies, *Colloids Surf., A*, 2014, **45**, 172–180.

39 A. Boyd, L. D. Randolph, L. Rutledge and B. J. Meenan, Strontium substituted hydroxyapatite coatings deposited *via* a co-deposition sputter technique, *Mater. Sci. Eng., C*, 2015, **46**, 290–300.

40 A. Boyd, L. Rutledge, L. D. Randolph, I. Mutreja and B. J. Meenan, The deposition of strontium-substituted hydroxyapatite coatings, *J. Mater. Sci.: Mater. Med.*, 2015, **26**, 1–14.

41 M. Mehrali, A. R. Akhiani, S. Talebian, M. Mehralia, S. T. Latibari and A. Dolatshahi-Pirouz, Electrophoretic deposition of calcium silicate reduced grapheneoxide composites on titanium substrate, *J. Eur. Ceram. Soc.*, 2016, **36**, 319e332.

42 F. Zuleta, P. A. Velasquez, A. De and P. N. Aza, In vitro characterization of laser ablation pseudowollastonite coating, *Mater. Sci. Eng., C*, 2011, **31**, 377–383.

43 M. Sarraf, B. Abdul Razak, A. Dabbagh, B. Nasiri-Tabrizi, N. H. Abu Kasim and W. J. Basirun, Optimizing PVD conditions for electrochemical anodization growth of well adherent Ta_2O_5 nanotubes on Ti-6Al-4V alloy, *RSC Adv.*, 2016, **82**, 78999–79015.

44 Y. Huang, X. J. Zhang, H. L. Zhang, H. X. Qiao, X. Y. Zhang, T. J. Jia, S. G. Han, Y. Gao, H. Y. Xiao and H. J. Yang, Fabrication of silver- and strontium-doped hydroxyapatite/TiO_2 nanotube bilayer coatings for enhancing bactericidal effect and osteoinductivity, *Ceram. Int.*, 2017, **43**, 992–1007.

45 Y. J. Yan, X. J. Zhang, Y. Huang, Q. Q. Ding and X. F. Pang, Antibacterial and bioactivity of silver substituted hydroxyapatite/TiO_2 nanotube composite coatings on titanium, *Appl. Surf. Sci.*, 2014, **314**, 348–357.

46 L. Xia, B. Wang, P. Ding, S. Liu, Z. Zhou and J. Yu, In vitro and in vivo studies of surface-structured implants for bone formation, *Int. J. Nanomed.*, 2012, **7**, 4873–4881.

47 A. Vladescu, S. C. Padmanabhan, F. Ak Azem, M. Braic, I. Titorencu, I. Birlik, M. A. Morris and V. Braic, Mechanical properties and biocompatibility of the sputtered Ti doped hydroxyapatite, *J. Mech. Behav. Biomed. Mater.*, 2016, **63**, 314–325.

48 N. Eliaz, S. Shmueli, I. Shur, D. Benayahu, D. Aronov and G. Rosenman, The effect of surface treatment on the surface texture and contact angle of electrochemically deposited hydroxyapatite coating and on its interaction with bone-forming cells, *Acta Biomater.*, 2009, **5**, 3178–3191.

49 F. Sima, C. Ristoscu, N. Stefan, G. Dorcioman, I. N. Mihailescu, L. E. Sima, S. M. Petrescu, E. Palcevskis, J. Krastins and I. Zalite, Shallow hydroxyapatite coatings pulsed laser deposited onto Al_2O_3 substrates with controlled porosity: correlation of morphological characteristics with in vitro testing results, *Appl. Surf. Sci.*, 2009, **255**, 5312–5317.

50 D. M. Vranceanu, C. M. Cotrut, M. Bramowicz, I. Titorencu, S. Kulesza, A. Kiss, A. Berbecaru, V. Pruna, M. Branzei and A. Vladescu, Osseointegration of sputtered SiC-added hydroxyapatite for orthopaedic applications, *Ceram. Int.*, 2016, **42**, 10085–10093.

51 Y. Liu, Z. Dang, Y. Wang, J. Huang and H. Li, Hydroxyapatite/graphene-nanosheet composite coatings deposited by vacuum cold spraying for biomedical applications: inherited nanostructures and enhanced properties, *Carbon*, 2013, **67**, 250–259.

52 M. Mehrali, A. R. Akhiani, S. Talebian, M. Mehrali, S. T. Latibari, A. Dolatshahi-Pirouz and H. S. C. Metselaar, Electrophoretic deposition of calcium silicate-reduced graphene oxide composites on titanium substrate, *J. Eur. Ceram. Soc.*, 2016, **36**, 319–332.

53 K. Liu, Y. Tian and L. Jiang, Bio-Inspired Superoleophobic and Smart Materials: Design, Fabrication, and Application, *Prog. Mater. Sci.*, 2013, **58**, 503–564.

54 X. Lin, F. Lu, Y. Chen, N. Liu, Y. Cao, L. Xu, Y. Wei and L. Feng, One-Step Breaking and Separating Emulsion by Tungsten Oxide Coated Mesh, *ACS Appl. Mater. Interfaces*, 2015, **7**, 8108–8113.

55 ISO, *Implants for Surgery-Hydroxyapatite-Part 4: Determination of Coating Adhesion Strength*, ISO 13779-4, 2002.

56 S. Ahmadi, I. Mohammadi and S. K. Sadrnezhaad, Hydroxyapatite based and anodic titania nanotube biocomposite coatings: fabrication, characterization and electrochemical behavior, *Surf. Coat. Technol.*, 2016, **287**, 67–75.

57 A. Kodama, S. Bauer, A. Komatsu, H. Asoh, S. Ono and P. Schmuki, Bioactivation of titanium surfaces using coatings of TiO_2 nanotubes rapidly pre-loaded with synthetic hydroxyapatite, *Acta Biomater.*, 2009, **5**, 2322–2330.

58 M. Sarraf, A. Dabbagh, B. A. Razaka, B. Nasiri-Tabrizi, H. R. M. Hosseini, S. Saber-Samandari, N. H. A. Kasimf, L. K. Yean and N. L. Sukiman, Silver oxide nanoparticles-decorated tantala nanotubes for enhanced antibacterial activity and osseointegration of Ti6Al4V, *Mater. Des.*, 2018, **154**, 28–40.

59 C. Zhao, P. Hou, J. Ni, P. Han, Y. Chai and X. Zhang, Ag-incorporated FHA coating on pure Mg: Degradation and in vitro antibacterial properties, *ACS Appl. Mater. Interfaces*, 2016, **8**, 5093–5103.

60 W. Z. Yu, Y. Zhang, X. Liu, Y. Xiang, Z. Li and S. Wu, Synergistic antibacterial activity of multi components in

lysozyme/chitosan/silver/hydroxyapatite hybrid coating, *Mater. Des.*, 2018, **139**, 351–362.

61 A. Ewald, D. Hosel, S. Patel, L. M. Grover, J. E. Barralet and U. Gbureck, Silver-Doped Calcium Phosphate Cements with Antimicrobial Activity, *Acta Biomater.*, 2011, **7**, 4064–4070.

62 Y. Chen, X. Zheng, Y. Xie, H. Ji, C. Ding, H. Li and K. Dai, Silver Release from Silver-Containing Hydroxyapatite Coatings, *Surf. Coat. Technol.*, 2010, **205**, 1892–1896.

63 L. Fathyunes and J. Khalil-Allafi, Characterization and corrosion behavior of grapheme oxide-hydroxyapatite composite coating applied by ultrasound-assisted pulse electrodeposition, *Ceram. Int.*, 2017, DOI: 10.1016/j.ceramint.2017.07.113.

64 D. Nancy and N. Rajendran, Vancomycin incorporated chitosan/gelatin coatings coupled with TiO_2–SrHAP surface modified cp-titanium for osteomyelitis treatment, *Surf. Coat. Technol.*, 2018, **110**, 197–205.

65 Y. Zhao, H. Cao, H. Qin, T. Cheng, S. Qian, M. Cheng, X. Peng, J. Wang, Y. Zhang, G. Jin, X. Zhang, X. Liu and P. K. Chu, Balancing the osteogenic and antibacterial properties of titanium by codoping of Mg and Ag: an in vitro and in vivo study, *ACS Appl. Mater. Interfaces*, 2015, **7**, 17826–17836.

66 B. Das, S. K. Dash, D. Mandal, T. Ghosh, S. Chattopadhyay, S. Tripathy, S. Das, S. K. Dey, D. Das and S. Roy, Green synthesized silver nanoparticles destroy multidrug resistant bacteria *via* reactive oxygen species mediated membrane damage, *ACS Nano*, 2017, **11**, 9010–9021.

67 B. Das, S. K. Dash, D. Mandal, T. Ghosh, S. Chattopadhyay, S. Tripathy, S. Das, S. K. Dey, D. Das and S. Roy, Green synthesized silver nanoparticles destroy multidrug resistant bacteria *via* reactive oxygen species mediated membrane damage, *Arabian J. Chem.*, 2017, **10**, 862–876.

68 L. Zhao, H. Wang, K. Huo, L. Cui, W. Zhang, H. Ni, Y. Zhang, Z. Wu and P. K. Chu, Antibacterial nano-structured titania coating incorporated with silver nanoparticles, *Biomaterials*, 2011, **32**, 5706–5716.

69 A. Agarwal, K. M. Guthrie, C. J. Czuprynski, M. J. Schurr, J. F. McAnulty, C. J. Murphy and N. L. Abbott, Polymeric multilayers that contain silver nanoparticles can be stamped onto biological tissues to provide antibacterial activity, *Adv. Funct. Mater.*, 2011, **21**, 1863–1873.

70 P. J. Marie, P. Ammann, G. Boivin and C. Rey, Mechanisms of action and therapeutic potential of strontium in bone, *ACS Nano*, 2017, **11**, 11250–11263.

71 E. L. Zhang and C. M. Zou, Porous titanium and silicon-substituted hydroxyapatite biomodification prepared by a biomimetic process: characterization and in vivo evaluation, *Adv. Mater.*, 2018, **30**, 1801808.

72 P. J. Marie, P. Ammann, G. Boivin and C. Rey, Mechanisms of action and therapeutic potential of strontium in bone, *Calcif. Tissue Int.*, 2001, **69**, 121–129.

73 E. L. Zhang and C. M. Zou, Porous titanium and silicon-substituted hydroxyapatite biomodification prepared by a biomimetic process: characterization and in vivo evaluation, *Acta Biomater.*, 2009, **5**, 1732–1741.

74 C. J. Chung and H. Y. Long, Systematic strontium substitution in hydroxyapatite coatings on titanium *via* micro-arc treatment and their osteoblast/osteoclast responses, *Acta Biomater.*, 2011, **7**, 4081–4087.

75 A. M. Pietak, J. W. Reid, M. J. Stott and M. Sayer, Silicon substitution in the calcium phosphate bioceramics, *Biomaterials*, 2007, **28**, 4023–4032.

76 E. S. Thian, J. Huang, S. M. Best, Z. H. Barber, R. A. Brooks, N. Rushton and W. Bonfield, The response of osteoblasts to nanocrystalline silicon-substituted hydroxyapatite thin films, *Biomaterials*, 2006, **27**, 2692–2698.

77 J. Braux, F. Velard, C. Guillaume, S. Bouthors, E. Jallot, J. M. Nedelec, D. Laurent-Maquin and P. Laquerriere, A new insight into the dissociating effect of strontium on bone resorption and formation, *Acta Biomater.*, 2011, **7**, 2593–2603.

78 P. S. Gomes, C. Botelho, M. A. Lopes, J. D. Santos and M. H. Fernandes, Evaluation of human osteoblastic cell response to plasma-sprayed silicon-substituted hydroxyapatite coatings over titanium substrates, *J. Biomed. Mater. Res., Part B*, 2010, **94**, 337–346.

79 W. E. Cabrera, I. Schrooten, M. E. De Broe and P. C. D. Haese, Strontium and bone, *J. Bone Miner. Res.*, 1999, **14**, 661–668.

80 K. Schwarz, A bound form of silicon in glycosaminoglycans and polyuronides, *Proc. Natl. Acad. Sci. U. S. A.*, 1973, **70**, 1608–1612.

81 K. Lin, P. Liu, W. Zhang, L. Wei, Z. Zou, Y. Qian, Y. Shen and J. Chang, Strontium substituted hydroxyapatite porous microspheres: surfactant-free hydrothermal synthesis, enhanced biological response and sustained drug release, *Chem. Eng. J.*, 2013, **222**, 49–59.

82 S. C. Skoryna, Metabolic aspects of the pharmacologic use of trace elements in human subjects with specific reference to stable strontium, *Trace Subst. Environ. Health*, 1984, **18**, 3–20.

83 J. Li, Y. Liu, L. Hermansson and R. Söremark, Evaluation of Biocompatibility of Various Ceramic Powders with Human Fribroblasts in vivo, *Clin. Mater.*, 1993, **12**, 197–201.

84 P. N. Lim, L. Chang, B. Y. Tay, V. Guneta, C. Choong, B. Ho and E. S. Thian, Proposed mechanism of antibacterial action of chemically modified apatite for reduced bone infection, *ACS Appl. Mater. Interfaces*, 2014, **6**, 17082–17092.

85 Z. Yin, X. Wang, X. Wang, N. Zhang, L. Chen, H. Qu, J. Chang, Z. Ren and K. Lin, Facile Synthesis of Element-Substituted Hydroxyapatite Whiskers Using α-Tricalcium Phosphate as Precursors, *Int. J. Appl. Ceram. Technol.*, 2015, **12**, 1000–1007.

86 N. Zhang, W. Liu, H. Zhu, L. Chen, K. Lin and J. Chang, Tailoring Si-substitution level of Si-hydroxyapatite nanowires *via* regulating Si-content of calcium silicates as hydrothermal precursors, *Ceram. Int.*, 2014, **40**, 11239–11243.

87 N. Zhang, D. Zhai, L. Chen, Z. Zou, K. Lin and J. Chang, Hydrothermal synthesis and characterization of Si and Sr co-substituted hydroxyapatite nanowires using strontium containing calcium silicate as precursors, *Mater. Sci. Eng., C*, 2014, **37**, 286–291.

